Monthly Notices
of the
ROYAL ASTRONOMICAL SOCIETY

MNRAS **468,** 4675–4690 (2017)
Advance Access publication 2017 April 10

doi:10.1093/mnras/stw3217

WISDOM Project – II. Molecular gas measurement of the supermassive black hole mass in NGC 4697

Timothy A. Davis,[1⋆] Martin Bureau,[2] Kyoko Onishi,[3,4] Michele Cappellari,[2] Satoru Iguchi[3,4] and Marc Sarzi[5]

[1]*School of Physics & Astronomy, Cardiff University, Queens Buildings, The Parade, Cardiff CF24 3AA, UK*
[2]*Sub-department of Astrophysics, Department of Physics, University of Oxford, Denys Wilkinson Building, Keble Road, Oxford OX1 3RH, UK*
[3]*Department of Astronomical Science, SOKENDAI (The Graduate University of Advanced Studies), Mitaka, Tokyo 181-8588, Japan*
[4]*National Astronomical Observatory of Japan, Mitaka, Tokyo 181-8588, Japan*
[5]*Centre for Astrophysics Research, University of Hertfordshire, Hatfield, Hertfordshire, AL1 9AB, UK*

Accepted 2017 March 14. Received 2016 December 6; in original form 2016 October 24

ABSTRACT

As part of the mm-Wave Interferometric Survey of Dark Object Masses (WISDOM) project, we present an estimate of the mass of the supermassive black hole (SMBH) in the nearby fast-rotating early-type galaxy NGC 4697. This estimate is based on Atacama Large Millimeter/submillimeter Array (ALMA) cycle-3 observations of the ^{12}CO(2–1) emission line with a linear resolution of 29 pc (0.53 arcsec). We find that NGC 4697 hosts a small relaxed central molecular gas disc with a mass of 1.6×10^7 M$_\odot$, co-spatial with the obscuring dust disc visible in optical *Hubble Space Telescope* imaging. We also resolve thermal 1 mm continuum emission from the dust in this disc. NGC 4697 is found to have a very low molecular gas velocity dispersion, $\sigma_{\rm gas} = 1.65^{+0.68}_{-0.65}$ km s^{-1}. This seems to be partially because the giant molecular cloud mass function is not fully sampled, but other mechanisms such as chemical differentiation in a hard radiation field or morphological quenching also seem to be required. We detect a Keplerian increase of the rotation of the molecular gas in the very centre of NGC 4697, and use forward modelling of the ALMA data cube in a Bayesian framework with the KINematic Molecular Simulation (KINMS) code to estimate an SMBH mass of $(1.3^{+0.18}_{-0.17}) \times 10^8$ M$_\odot$ and an *i*-band mass-to-light ratio of $2.14^{+0.04}_{-0.05}$ M$_\odot$/L$_\odot$ (at the 99 per cent confidence level). Our estimate of the SMBH mass is entirely consistent with previous measurements from stellar kinematics. This increases confidence in the growing number of SMBH mass estimates being obtained in the ALMA era.

Key words: galaxies: elliptical and lenticular, cD – galaxies: individual: NGC 4697 – galaxies: ISM – galaxies: kinematics and dynamics – galaxies: nuclei.

1 INTRODUCTION

Supermassive black holes (SMBHs) are some of the most enigmatic objects in our Universe. Evidence has mounted over many years that the majority of massive galaxies have a large SMBH in their centre (see e.g. the review by Kormendy & Ho 2013). Although these objects are massive (having typical masses of 10^6–10^{10} M$_\odot$), their spatial extents are small compared to their host galaxies (with event horizons on au scales and their gravitational spheres of influence typically $\ll$100 pc). Despite these small sizes, strong correlations between galaxy properties and the masses of the black holes (e.g. Magorrian et al. 1998; Gebhardt et al. 2000; Graham et al. 2001; Gültekin et al. 2009; McConnell & Ma 2013) suggest that SMBHs play a key role in shaping the evolution of massive galaxies.

Theoretical models of galaxy formation are able to reproduce these correlations between galaxies and their SMBHs, and suggest that this co-evolution likely involves self-regulation mechanisms. One possible process that could regulate both SMBH and galaxy growth is feedback from an active galactic nucleus (AGN; Silk & Rees 1998; Di Matteo et al. 2008). Understanding this co-evolution, and how it changes in galaxies of different masses/morphological types, is vital to understand the impact of SMBHs on galaxy evolution (e.g. Schawinski et al. 2007).

To make progress on this issue observationally, it is crucial to have accurate, well-calibrated ways to measure SMBH masses in a large number of galaxies. A variety of methods exist to estimate the black hole mass for actively accreting objects (e.g. reverberation mapping, Peterson et al. 1998; single epoch line estimates,

⋆ E-mail: DavisT@cardiff.ac.uk

McGill et al. 2008; etc.). However, the most reliable method of SMBH mass measurement is usually thought to be spatially resolved dynamics. In our own Milky Way, this is possible using the resolved motion of individual stars (Ghez et al. 2008; Gillessen et al. 2009), while for external galaxies measurements can be made using integrated stellar light both with long-slit (e.g. Dressler & Richstone 1988; Magorrian et al. 1998; Gebhardt et al. 2003) and integral-field spectroscopy (e.g. Verolme et al. 2002; Cappellari et al. 2009). Interstellar gas also provides several complimentary tracers of galaxy potentials. The best of these is maser emission from circumnuclear accretion discs that, when present, allows exquisite SMBH mass estimates (e.g. Miyoshi et al. 1995; Greene et al. 2010). Unfortunately, suitable systems are quite rare. Ionized gas can also be used to estimate SMBH masses after suitable corrections for asymmetric drift have been applied (e.g. Ferrarese, Ford & Jaffe 1996; Sarzi et al. 2001; Neumayer et al. 2007).

In the last few years, substantial improvements in observational capabilities have also allowed molecular gas to be used to estimate SMBH masses. Davis et al. (2013b) presented the first measurement of this type, estimating the mass of the SMBH in the Virgo cluster fast-rotating early-type galaxy (ETG) NGC 4526. Davis (2014) presented a figure of merit for this technique, and showed that with the Atacama Large Millimeter/submillimeter Array (ALMA) this method should allow SMBH mass measurements in thousands of galaxies across the Universe (see also Hezaveh 2014 for the prospects of its use in lensed galaxies at very high redshifts). Onishi et al. (2015) presented the first use of this technique in a spiral galaxy (NGC 1097), while Barth et al. (2016a,b) showed its power to resolve the Keplerian increase in velocity around black holes directly.

As a result, building on some of these small pilot projects (Davis et al. 2013b; Onishi et al. 2015), we have recently started the mm-Wave Interferometric Survey of Dark Object Masses (WISDOM) project. This project aims to benchmark and test the molecular gas dynamics method, develop tools and best practice, and exploit the growing power of ALMA to better populate and thus constrain SMBH–galaxy scaling relations. The first paper in this series discussed in detail the tools and fitting procedures developed so far, and presented a mass measurement in the nearby fast-rotating ETG NGC 3665 using CARMA data (Onishi et al. 2017).

In this work, we present ALMA cycle-3 observations of the molecular gas disc in the centre of the fast-rotating elliptical galaxy NGC 4697 (see Fig. 1), and use these to estimate the SMBH mass. The SMBH mass in this object is known from previous work using stellar kinematics (Gebhardt et al. 2003; Schulze & Gebhardt 2011), so our new observations allow us to conduct a vital cross-check between these two methods.

In Section 2 of this paper, we describe our target. In Section 3, we present our ALMA observations, and describe the derived data products. In Section 4, we discuss our dynamical modelling method. In Section 5, we discuss our results and compare our SMBH mass measurement with those made by other authors. Finally, we conclude in Section 6. Throughout this paper, we assume a distance of 11.4 ± 1.1 Mpc for NGC 4697 (Cappellari et al. 2011), as derived from surface brightness fluctuation (SBF) measurements in Tonry et al. (2001). At this distance, 1 arcsec corresponds to a physical scale of 55 pc.

2 TARGET

NGC 4697 is the brightest galaxy in a poor group (the NGC 4697 group) with five other lower mass members (Madore, Freedman & Bothun 2004). Integral-field observations reveal that despite its optical classification as an E6 elliptical, this object is a fast rotator (Emsellem et al. 2011). Fig. 1 shows that it also has a nuclear disc of dust visible in *Hubble Space Telescope* (*HST*) imaging. NGC 4697 has a total stellar mass of 1.2×10^{11} $M_\odot$, and a luminosity-weighted stellar velocity dispersion within one effective radius of $\sigma_e = 169$ km s^{-1} (Cappellari et al. 2013a).

Both Gebhardt et al. (2003) and Schulze & Gebhardt (2011) have estimated the SMBH mass in NGC 4697, using *HST* long-slit observations to model the stellar kinematics. They found a black hole mass of $\approx 1.6 \times 10^8$ $M_\odot$. There is radio continuum emission from the central regions of this galaxy, leading to its classification as a low-luminosity AGN. The black hole does not seem to be very active, however, with an upper limit on the Eddington ratio from combined radio and X-ray observations of 10^{-9} (Sarazin, Irwin & Bregman 2001; Wrobel, Terashima & Ho 2008).

The star formation rate (SFR) of NGC 4697 is not well constrained but is very low. Davis et al. (2014) used 22 μm emission to estimate an upper limit to the SFR of 0.06 $M_\odot$ yr^{-1}, and caution that the majority of this flux is likely to arise from the circumstellar envelopes around evolved stars. Assuming all the radio continuum emission in this object comes from star formation sets a more stringent upper limit of 0.006 $M_\odot$ yr^{-1} (Brown et al. 2011). Ford & Bregman (2013) used *HST* ultraviolet imaging to detect young stellar clusters in this object, and used these to estimate an SFR of 4.6×10^{-4} $M_\odot$ yr^{-1}. We note however that Ford & Bregman (2013) were unable to probe deep inside the dust disc, where the majority of the molecular gas in this system is, so we consider this measurement a lower limit to the total SFR.

3 ALMA DATA

The ^{12}CO(2–1) line in NGC 4697 was observed with ALMA on 2016 May 1 as part of the WISDOM project (programme 2015.1.00598.S). The total integration time on source was 574 s, observed as a single track. The C36-3 antenna configuration was used, yielding sensitivity to emission on scales up to 17 arcsec. An 1850 MHz correlator window was placed over the CO(2–1) line, yielding a continuous velocity coverage of ≈2000 km s^{-1} with a raw velocity resolution of ≈1 km s^{-1}, sufficient to properly cover and sample the line. Three additional 2 GHz wide low-resolution correlator windows were simultaneously used to detect continuum emission.

The raw ALMA data were calibrated using the standard ALMA pipeline, as provided by the ALMA regional centre staff. Amplitude and bandpass calibration were performed using J1256−0547. The atmospheric phase offsets present in the data were determined using J1246−0730 as a phase calibrator.

We then used the Common Astronomy Software Applications (CASA) package to combine and image the resultant visibility file, producing a three-dimensional RA–Dec.–velocity data cube (with velocities determined with respect to the rest frequency of the ^{12}CO(2–1) line). In this work, we primarily use data with a channel width of 10 km s^{-1}, but in Section 4.3 we re-image the calibrated visibilities with a channel width of 3 km s^{-1}. In both cases, pixels of 0.1 arcsec × 0.1 arcsec were chosen as a compromise between spatial sampling and resolution, resulting in approximately 5 pixels across the beam major axis.

The data presented here were produced using Briggs weighting with a robust parameter of 0.5, yielding a synthesized beam of 0.54 arcsec × 0.52 arcsec at a position angle of −22° (a linear resolution of ≈30 × 29 pc). Continuum emission was detected,

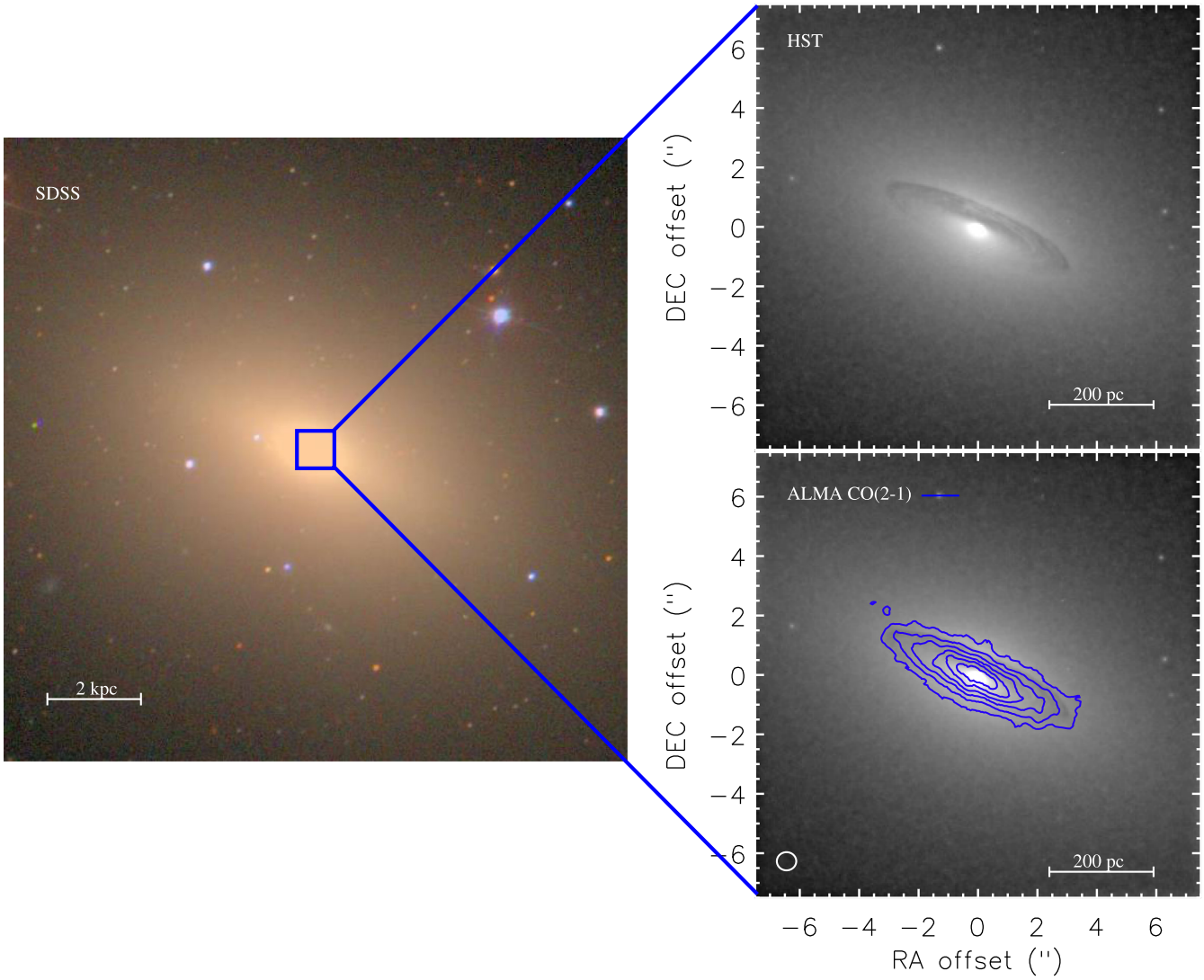

Figure 1. Left-hand panel: SDSS three-colour (*gri*) image of NGC 4697, 4 arcmin × 4 arcmin (13.2 kpc × 13.2 kpc) in size. Right-hand panel, top: unsharp-masked *HST* Advanced Camera for Surveys (ACS) *F*850*LP* image of an 825 pc × 825 pc region (indicated in blue in the left-hand panel) around the nucleus, revealing a clear central dust disc. Right-hand panel, bottom: as above, but overlaid with blue ^{12}CO(2–1) integrated intensity contours from our ALMA observations. The synthesized beam (0.54 arcsec × 0.52 arcsec, 30 × 29 pc) is shown as a white ellipse in the bottom-left corner of the panel.

measured over the full line-free bandwidth and then subtracted from the data in the *uv* plane using the CASA task `uvcontsub`. The achieved continuum root-mean-square (rms) noise is 35 μJy. The continuum-subtracted dirty cubes were cleaned in regions of source emission (identified interactively) to a threshold equal to the rms noise of the dirty channels. The clean components were then added back and re-convolved using a Gaussian beam of full width at half-maximum (FWHM) equal to that of the dirty beam. This produced the final, reduced and fully calibrated ^{12}CO(2–1) data cubes of NGC 4697, with an rms noise level of 1.1 mJy beam^{-1} in each 10 km s^{-1} channel (or 2.1 mJy beam^{-1} in each 3 km s^{-1} channel).

3.1 Line emission

The clean fully calibrated data cube was used to create our final data products. The observed channel maps are presented in Appendix A. A major-axis position–velocity diagram (PVD; taken along a position angle of 246°, as determined below, and with a width of 5 pixels) was extracted, and is shown in Fig. 2.

Zeroth moment (integrated intensity), first moment (mean velocity) and second moment (velocity dispersion) maps of the detected line emission were then created using a masked moment technique. A copy of the clean data cube was first Gaussian-smoothed spatially (with an FWHM equal to that of the synthesized beam), and then Hanning-smoothed in velocity. A three-dimensional mask was then defined by selecting all pixels above a fixed flux threshold of 1.5σ, adjusted to recover as much flux as possible in the moment maps while minimizing the noise. The moment maps were then created using the unsmoothed cubes within the masked regions only. The moments are presented in Section 4.3.

We clearly detect a regular disc of molecular gas in NGC 4697, with a size of ≈390 pc × 100 pc in projection. This gas is regularly rotating and lies coincident with the dust disc visible in *HST* imaging (see Fig. 1). A central enhancement of the gas velocity is clearly present around the galaxy centre, which is likely to be the Keplerian increase of the gas velocity around a putative SMBH (see Fig. 2).

The velocity dispersion in this molecular disc seems very low, with clear channelization present in the upper envelope of the PVD.

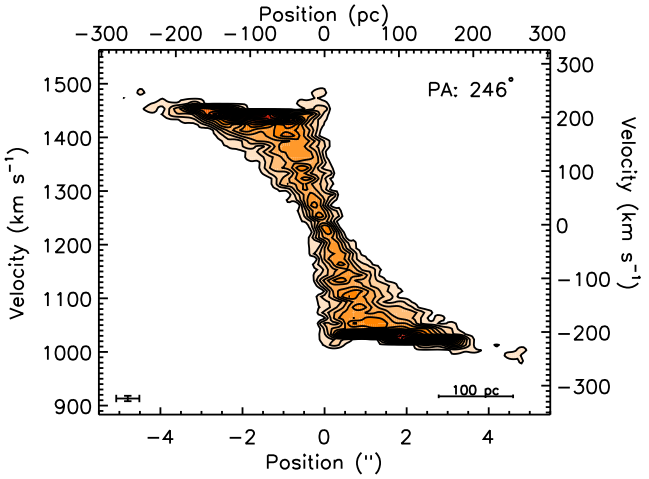

Figure 2. PVD of the ^{12}CO(2–1) emission in NGC 4697, extracted along the kinematic major axis. The synthesized beam size (along the major axis) and spectral resolution of our observations are indicated as an error bar in the bottom-left corner. A steep increase of the gas velocity is visible in the galaxy centre, arising from material orbiting around the central SMBH.

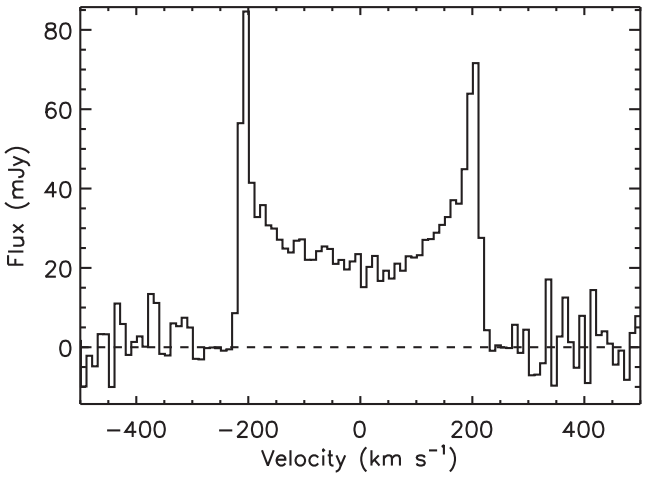

Figure 3. Integrated ^{12}CO(2–1) spectrum extracted from our observed data cube in an 8 arcsec × 4 arcsec (440 pc × 220 pc) region around the galaxy centre, covering all the detected emission. A dashed line indicates the zero flux level. The spectrum shows the classic double-horn shape of a rotating disc.

This suggests that the velocity dispersion is small compared with our channel width of 10 km s^{-1}. We note that the large line widths visible in Fig. 2 (and in the second moment maps presented in Section 4.2) are primarily due not to the intrinsic velocity dispersion, but to beam smearing over the velocity gradient at the galaxy centre and the line-of-sight integration through the fairly edge-on disc. This is discussed further in Sections 4.3 and 5.

Fig. 3 shows the integrated ^{12}CO(2–1) spectrum of NGC 4697, with the classic double-horn shape of a rotating disc. The total flux is 13.27 ± 0.07 ± 1.3 Jy km s^{-1} (where the second uncertainty is systematic and accounts for the ≈10 per cent flux calibration uncertainty in the ALMA data). From this measurement, assuming a typical CO(2–1)/CO(1–0) ratio of 0.8 (Bigiel et al. 2008) and a Galactic $X_{\rm CO}$ conversion factor (as in Young et al. 2011), we estimate a total H_2 mass of (1.62 ± 0.01 ± 0.36) × 10^7 M$_\odot$. The systematic uncertainty quoted here on the H_2 mass includes a contribution from both the flux calibration uncertainty and the uncertainty in our assumed distance. These uncertainties are included as a second error bar where appropriate in the rest of this section.

Like many ETGs, NGC 4697 seems to have a lower SFR per unit gas mass (also known as the star formation efficiency, SFE) than nearby spiral galaxies (Saintonge et al. 2011; Davis et al. 2014). As described above, the SFR of this system is hard to constrain but likely lies in the range $4.6 \times 10^{-4} \lesssim {\rm SFR} \lesssim 0.006$ M$_\odot$ yr^{-1}. The specific SFR (SFR per unit stellar mass) of NGC 4697 is thus very low, between 5×10^{-14} and 4×10^{-15} yr^{-1}. Using our total H_2 mass, we calculate that the SFE is between 2.8×10^{-11} and 3.7×10^{-10} yr^{-1}. This equates to a gas depletion time of between 2.7 and 35 Gyr, lower than in local spirals (and indeed galaxies of all types with a similar stellar mass) that typically have depletion times of ≈2 Gyr (Bigiel et al. 2011; Saintonge et al. 2011).

3.2 Continuum emission

As mentioned above, continuum emission was detected in NGC 4697. The emission is spatially resolved, as shown in the left-hand panel of Fig. 4. A central point source is present, but flux is also detected in an extended structure aligned with the dust disc visible in the *HST* image. Given that the elongation of the continuum emission is very similar to that of the molecular gas disc itself (as shown by the grey contours in the left-hand panel of Fig. 4), we consider it unlikely that this emission is from a background object. Aperture photometry allows us to estimate a total flux of 2.1 ± 0.1 ± 0.2 mJy.

Given the evidence for a low-luminosity AGN in NGC 4697, we wish to determine if this emission is non-thermal in origin (i.e. a central AGN point source plus emission from a jet) or if it is consistent with thermal emission from dust. The right-hand panel of Fig. 4 shows the spectral energy distribution (SED) of this object from 1 GHz to 10 THz. *Herschel* and *Spitzer Space Telescope* data are taken from the Herschel Almanac of Early Types (HEART) project of Smith et al. (in preparation), while homogenized radio and infrared archival data were taken from the NASA Extragalactic Database[1] (NED).

A simple SED model was fitted to these data points using the χ^2 minimization routines `MPFIT` (Markwardt 2009). The far-infrared emission was modelled as a modified blackbody:

$$S_\nu = \frac{\kappa_\nu M_{\rm d} B(\nu, T_{\rm d})}{D^2}, \quad (1)$$

where $M_{\rm d}$ is the dust mass with dust temperature $T_{\rm d}$, $B(\nu, T_{\rm d})$ is the Planck function and D is the distance to the galaxy. κ_ν is the dust absorption coefficient, described by a power law with dust emissivity index β such that $\kappa_\nu \propto \nu^\beta$. We here utilize an empirical κ_ν, $\kappa_{500\,\mu{\rm m}} = 0.051$ m^2 kg^{-1} and $\beta = 1.8$ (Clark et al. 2016).

In the radio regime, with only two data points available, we assume that the emission arises from synchrotron losses and can thus be represented by a power law. We fix the radio spectral index to −0.8 (as typically assumed for synchrotron from supernovae/star formation; Condon 1992). Although not well constrained, allowing the spectral index to vary would drive it to steeper values. We note that radio emission from AGN typically has a flatter spectral index, which would not agree with these data (e.g. Nyland et al. 2016).

With the parameters described above, we fit the HEART and literature data to obtain a best-fitting dust mass and temperature (along with the radio power-law normalization). We find that the

[1] http://ned.ipac.caltech.edu/

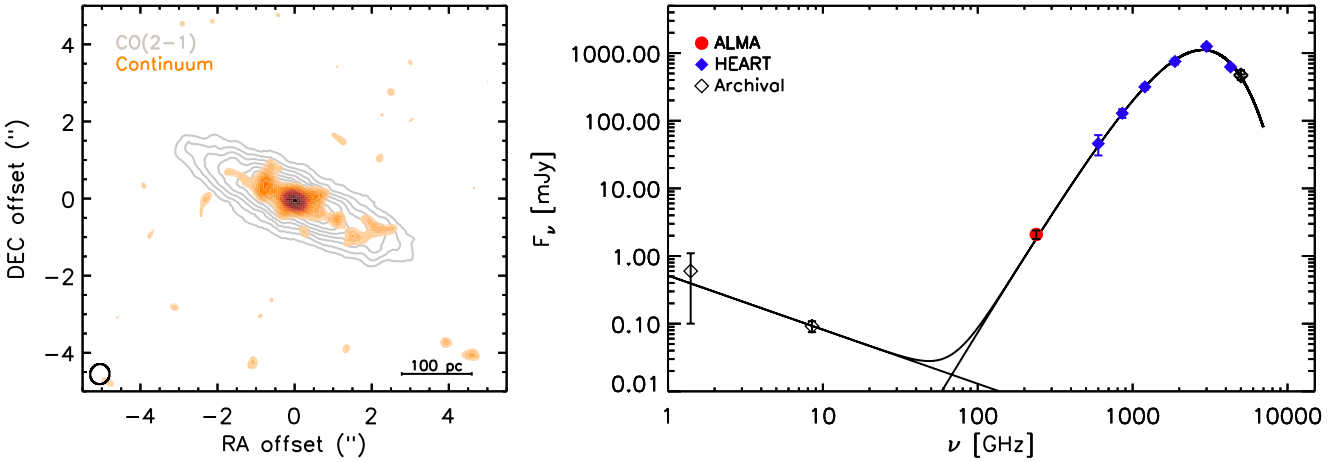

Figure 4. Left-hand panel: map of the 1 mm continuum emission from NGC 4697 (orange filled contours), overplotted on the CO(2–1) contours from Fig. 1 (grey). Right-hand panel: spectral energy distribution of NGC 4697, showing archival radio continuum and mid-infrared observations as black open diamonds, the HEART project reprocessed *Spitzer* and *Herschel* data as blue diamonds, and our total ALMA 1 mm continuum flux measurement as a red circle. The error bar on our ALMA measurement includes the systematic uncertainties as described in the text. The three largely overlapping black lines show the best-fitting SED and its infrared dust and radio synchrotron components. The ALMA continuum is consistent with arising entirely from the Rayleigh–Jeans tail of emission from dust.

data are well fitted with $M_{\rm d} = (2.8 \pm 0.2 \pm 1.0) \times 10^5$ M$_\odot$ and $T_{\rm d} = 28.7 \pm 0.4$ K, which agrees well with the values obtained by Smith et al. (in preparation). Our ALMA 1 mm continuum measurement, although not included in the fit, lies on the predicted SED. Including the ALMA data in the fit increases the dust mass and decreases the temperature very slightly, but these changes are not significant given our errors.

Overall, it seems that the millimetre continuum we detect is thermal in origin, and comes from the Rayleigh–Jeans tail of the dust emission. The morphology of the continuum source suggests that the AGN in this system is contributing to dust heating, but non-thermal emission is not important at this frequency.

Taking our dust mass estimate and combining it with our H_2 gas mass measured above, we derive a molecular gas-to-dust mass ratio of $58 \pm 7 \pm 6$. This is entirely consistent with a high metallicity in the gas phase, similar to the majority of relaxed ETGs (Smith et al. 2012).

4 METHOD AND RESULTS

In the above section, we detailed the properties of the data we obtained for NGC 4697. If we wish to fulfil the goals of this paper, however, we need to ascertain if the data are suitable for estimation of the SMBH mass. The formal sphere of influence (SOI) radius ($R_{\rm SOI}$) of the SMBH of a system is given by

$$R_{\rm SOI} = \frac{G M_{\rm BH}}{\sigma_*^2}, \quad (2)$$

where G is the gravitational constant, $M_{\rm BH}$ is the SMBH mass and σ_* is the stellar velocity dispersion. For our target with $M_{\rm BH} = 1.6 \times 10^8$ M$_\odot$ (Gebhardt et al. 2003; Schulze & Gebhardt 2011) and an effective σ_* of 169 km s^{-1} (Cappellari et al. 2013a), $R_{\rm SOI} = 27.1$ pc, similar to the spatial resolution of our observations. However, as Davis (2014) discusses in detail, for the molecular gas SMBH mass estimation method, the formal SOI criterion is not very meaningful. When using a method based on cold gas, the central velocity (and thus mass) profile of the galaxy becomes important.

Davis (2014) defined a figure of merit ($\Gamma_{\rm FOM}$) for such observations, which takes the above effects into account. $\Gamma_{\rm FOM}$ is equal to unity for a 1σ detection of the increased velocity due to an SMBH in the central beam of interferometric observations. For a robust determination of the SMBH mass, Davis (2014) suggests obtaining data for which $\Gamma_{\rm FOM} > 5$. We thus applied the figure of merit criterion, as detailed in equation 4 of Davis (2014), to our data:

$$\Gamma_{\rm FOM} = \frac{\sqrt{[v_{\rm gal}(r_\theta)^2 - \phi_{\rm BH}(r_\theta)]} - v_{\rm gal}(r_\theta)}{\delta v} \sin i, \quad (3)$$

where

$$\delta v = \sqrt{0.5({\rm CW})^2 + \delta v|^2_{\rm gal}}, \quad (4)$$

r_θ is the radius one synthesized beamwidth away from the nucleus along the galaxy major axis, $v_{\rm gal}$ is the velocity predicted from the luminous mass distribution (see below), $\phi_{\rm BH}$ is the gravitational potential of the SMBH, i is the inclination and δv is the velocity precision obtainable. Here we chose to include both the error caused by the finite channel width (CW) and that from uncertainties in the mass model ($\delta v|_{\rm gal}$).

For NGC 4697, our observational setup implies $\theta = 0.52$ arcsec (28.7 pc) and CW = 10 km s^{-1}. $\phi_{\rm BH}$ is calculated with $M_{\rm BH} = 1.6 \times 10^8$ M$_\odot$ as above. Ellipse fitting to the dust disc in the *HST* images yields $i = 76^\circ$. In this object $v_{\rm gal}(r_\theta) = 160$ km s^{-1}, calculated by multiplying the multi-Gaussian expansion (MGE) of Scott et al. (2013) with the mass-to-light ratio (M/L) of Cappellari et al. (2013a), and calculating the circular velocity as described in appendix A of Cappellari et al. (2002). $\delta v|_{\rm gal}$ is assumed to be ± 10 km s^{-1} (see Section 4.3). These parameters yield $\Gamma_{\rm FOM} = 5.9$, suggesting that we should be able to accurately constrain the SMBH mass in this system.

In the rest of this section, we therefore outline our method for estimating the SMBH mass and other physical parameters of NGC 4697 from the observed molecular gas kinematics.

4.1 Dynamical modelling

We used a forward modelling approach to estimate the black hole mass (and other physical parameters) of our source. We utilized

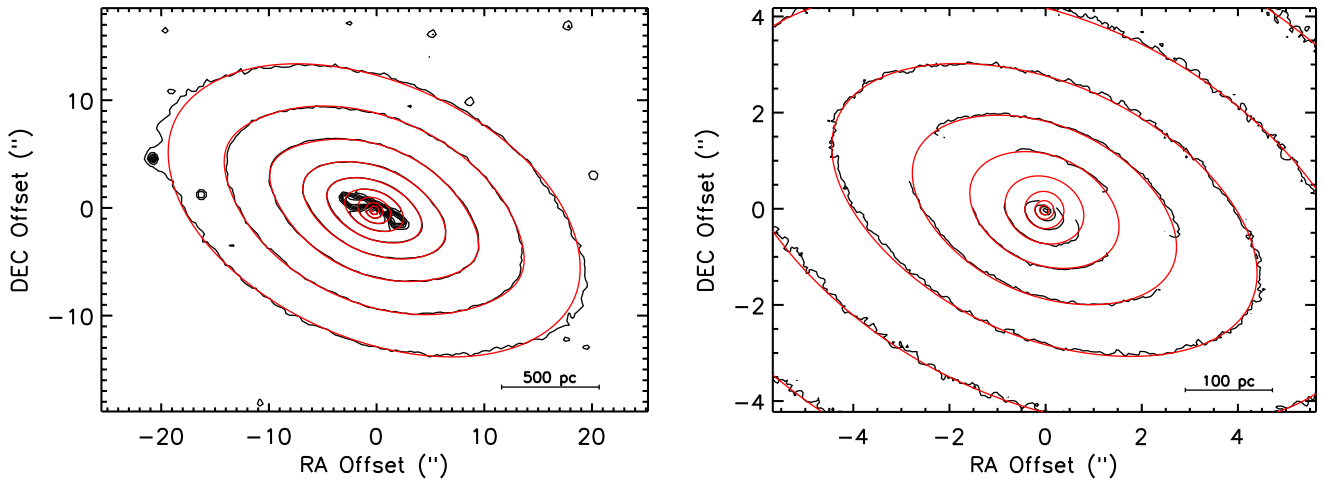

Figure 5. Our MGE model of NGC 4697 (red contours), overlaid on an *HST* *i*-band (ACS *F*850*LP*) image (black contours). The left-hand panel shows the whole galaxy, while the right-hand panel shows a zoom-in on the central region. The region masked due to dust is clearly visible to the north of the galaxy nucleus in the left-hand panel, and as breaks in the black contours in the right-hand panel.

the publicly available KINematic Molecular Simulation (KINMS[2]) mm-wave observation simulation tool of Davis et al. (2013a). This tool allows input guesses for the true gas distribution and kinematics and, taking into account the observational effects of beam smearing, spatial and velocity binning, disc thickness, gas velocity dispersion, etc., produces a simulated data cube that can be compared to observational data.

To determine the best-fitting model parameters and their uncertainties, we used the Markov chain Monte Carlo (MCMC) code KINMS_MCMC (Davis et al., in preparation), which couples to the KINMS routines and allows us to fit the data and obtain samples drawn from the Bayesian posterior probability distributions of the fitted parameters. This code fits the entire data cubes produced by interferometers rather than simply the PVD (as discussed in detail in Onishi et al. 2017). The simulated cubes use a synthesized beam, pixel size and velocity resolution identical to our observations.

4.1.1 Gas distribution

One of the inputs of the KINMS models is an arbitrarily parametrized function that describes the gas surface brightness distribution. At our resolution, the molecular gas disc of NGC 4697 is remarkably consistent with an exponential disc (that has also been shown to be appropriate for most ETGs; Davis et al. 2013a), so this simple form was adopted. In our modelling, the exponential disc scalelength was left as a free parameter, modified by the KINMS_MCMC code to obtain a good fit. Various other free parameters of the gas disc are also included in the model. These are the total flux, position angle and inclination of the gas disc, as well as its kinematic centre (in RA, Dec. and velocity). We find no evidence of a warp in this galaxy, so the inclination and position angle are each fitted as a single value valid throughout the disc.

4.1.2 Gas kinematics

The kinematics of the molecular gas contains contributions from both the luminous stellar mass and the SMBH. To remove the contribution of visible matter, and calculate the true mass of any dark object present at the centre of NGC 4697, we thus need to construct a luminous mass model. We note that dark matter, while important at larger galactocentric distances, is usually negligible at these radii. Indeed, Cappellari et al. (2013b) found that this object has a negligible dark matter fraction within one effective radius, and we are working well within this (at $<R_e/7$).

We parametrize the luminous matter distribution using an MGE (Emsellem, Monnet & Bacon 1994) model of the stellar light distribution, constructed using the MGE_FIT_SECTORS package[3] of Cappellari (2002). Our best-fitting MGE model is shown in Fig. 5 and is tabulated in Table 1. This was constructed from an *HST* Advanced Camera for Surveys (ACS) *F*850*LP* image (the longest wavelength available, to minimize dust extinction).

Under the Gaussian density distribution assumption, the model of the stellar light can be de-projected analytically given an inclination (the same as fitted by KINMS_MCMC). The light model then directly predicts the circular velocity of the gas caused by the luminous matter, via the stellar *M*/*L* (a free parameter of our model). The *M*/*L* derived is valid in the *F*850*LP* filter band, and is defined in the *HST* ACS system, although we abbreviate this to M/L_i here

Table 1. MGE parametrization of the galaxy light profile. The central unresolved Gaussian, indicated with a star, is removed to minimize the effect of the AGN on our kinematic fitting.

$\log_{10} I_j$ ($L_{\odot,i}$ pc^{-2}) (1)	$\log_{10} \sigma_j$ (arcsec) (2)	q_j (3)
*5.579	*−1.281	*0.932
4.783	−0.729	1.000
4.445	−0.341	0.863
4.239	−0.006	0.726
4.061	0.367	0.541
3.698	0.665	0.683
3.314	0.809	0.318
3.538	1.191	0.589

[2] https://github.com/TimothyADavis/KinMS

[3] http:purl.org/cappellari/software

Table 2. Best-fitting model parameters and uncertainties. Column 1 lists the fitted model parameters, while column 2 lists the associated prior. Priors are uniform in linear space (or in logarithmic space for the SMBH mass only). The posterior distribution of each parameter is quantified in columns 3–5 (see also Fig. 3). The *X*, *Y* and velocity offset nuisance parameters are defined relative to the ALMA data phase centre position (RA = 12:38:35.91, Dec. = −05:48:03.1, $V = 1241$ km s^{-1}). A star (⋆) indicates that this parameter is not well constrained by our data with 10 km s^{-1} channels, as discussed in detail in the text.

Parameter (1)	Search range (2)			Best fit (3)	Error (68 per cent conf.) (4)	Error (99 per cent conf.) (5)
Black hole:						
SMBH mass (10^8 $M_\odot$)	0.0006	→	63.0	1.26	−0.06, +0.03	−0.14, +0.18
Stellar M/L ($M_\odot/L_{\odot,i}$)	0.1	→	4.0	2.14	±0.02	−0.05, +0.04
Molecular gas disc:						
Position angle (°)	0.0	→	359.9	246.2	−0.2, +0.3	±0.7
Inclination (°)	72.0	→	89.0	76.1	−0.4, +0.5	±1.1
Scalelength (arcsec)	0.0	→	10.0	1.35	−0.06, +0.05	−0.18, +0.21
Velocity dispersion (km s^{-1})⋆	0.1	→	30.0	0.82	−0.63, +0.23	−0.76, +1.83
Nuisance parameters:						
Luminosity scaling	1.0	→	50.0	17.1	−0.8, +0.7	−1.9, +2.0
Centre *X* offset (arcsec)	−1.0	→	1.0	−0.10	±0.01	−0.04, +0.03
Centre *Y* offset (arcsec)	−1.0	→	1.0	−0.03	±0.01	−0.03, +0.02
Centre velocity offset (km s^{-1})	−20.0	→	20.0	0.15	−0.43, +0.35	−1.22, +1.25

for brevity. We note that NGC 4697 contains an AGN that likely contributes significantly to the unresolved point source at the galaxy centre. We subtract this point source by removing the innermost (spatially unresolved) Gaussian from our MGE model (as listed in Table 1). We note that including this point source would lower our derived SMBH mass by 0.1 dex, and we include this in our derived uncertainties. In any case, this would not significantly alter our results (as discussed in Section 5).

In this work, we always assume that the gas is in circular motion, and hence that the gas rotation velocity varies only radially. We do, however, also include a free parameter for the internal velocity dispersion of the gas, which is assumed to be spatially constant. The effects of deviations from circular motion and of allowing the velocity dispersion to vary radially are discussed in Section 4.3.

4.2 Bayesian analysis

As mentioned above, we use a Bayesian analysis technique to identify the best set of model parameters from our data cube. This allows us to obtain samples drawn from the posterior distribution of the 10 model parameters (see Table 2). A full description of this MCMC code will be published in Davis et al. (in preparation). In brief, we utilize an MCMC method with Gibbs sampling and adaptive stepping to explore the parameter space. This code has been cross-checked using a newly developed version of the KINMS routines in the PYTHON language (denoted by KINMSPY) coupled with the well-tested MCMC code EMCEE (Foreman-Mackey et al. 2013). These tests showed that our algorithm performs well, and finds the same best-fitting values and parameter ranges.

4.2.1 *Covariance matrix and likelihood*

As our data are approximately Nyquist sampled spatially, the synthesized beam induces strong correlations between neighbouring spaxels in the data cube. There are two possible approaches to deal with this issue: including the full covariance matrix when calculating the likelihood, or working in the *UV* plane where the data points are uncorrelated. In this work, we take the first approach, while the latter will be explored in a future work.

We are able to calculate the full covariance matrix analytically[4] as we know the synthesized beam shape. We summarize the basic method used below. In what follows, we assume that adjacent velocity channels are independent, and so the same two-dimensional covariance matrix can be used in each channel. Some smoothing is applied to raw velocity channels by the ALMA pipeline, but our assumption of independence is good as the channel width of the processed data is more than twice the raw instrumental channel width.

We assume that each channel of our data cube is formed from some 'true' image (I) where all pixels are uncorrelated, i.e. the flux in each pixel is a random variable independent of all other fluxes in the image. Any channel from this cube that is N_x by N_y pixels in size contains N_xN_y pixels, denoted by P_{ij}, where i runs from 1 to N_x and j from 1 to N_y. This pixel matrix can be represented as a vector composed of elements p_n, where $n = 1$ to $N_t \equiv N_xN_y$, where

$$p_{i+(j-1)N_x} = P_{ij}. \tag{5}$$

This 'true' image has been observed with a response function (B) that is oversampled by the pixel size. In our case, B is known to be isoplanatic (as the ALMA beam, to first order, is spatially invariant), and the observed data O thus arises from the discrete convolution

$$O = I * B. \tag{6}$$

Let us define the ALMA beam as an elliptical Gaussian with a fixed size and position angle ($\mathfrak{B}$). Within a channel of size N_x by N_y (as above), the beam $\mathfrak{B}_{ij}$ can be vectorized to $\mathfrak{B}_n$ using equation (5). This beam can be centred on any point p within the channel. In vectorized form, we denote this by $\mathfrak{b}_n(p)$. We use this beam as the response function, and map it to a response matrix R_{mn}, which is $N_xN_y \times N_xN_y$ in size. The columns of this matrix can be built up as

$$\begin{aligned} R_{0m} &= \mathfrak{b}_n(p=0), \\ R_{1m} &= \mathfrak{b}_n(p=1), \\ &\cdots \end{aligned} \tag{7}$$

[4] following the scheme outlined at http://web.ipac.caltech.edu/staff/fmasci/home/astro_refs/PixelNoiseCorrelation.pdf

The resulting response matrix is both sparse and diagonally banded. The covariance matrix ($\mathfrak{C}$) can then be calculated from this response matrix as

$$\mathfrak{C} = R^T R \sigma^2, \tag{8}$$

where σ is the rms noise of our data cube, estimated in central line-free regions of the cube. We have here assumed that the observational error in each pixel is the same (i.e. the rms noise in the data cube does not vary spatially). This is a reasonable assumption in the central region of the ALMA primary beam.

The resulting covariance matrix is large (up to 4096×4096 pixels for the fitting areas used in this paper), and it has a large condition number. As such, we do not invert it directly to calculate the likelihood, but instead introduce a modified Cholesky (LDL^T) factorization step (Gill, Murray & Wright 1981) to avoid loss of numerical precision when calculating the inverse ($\mathfrak{C}^{-1}$).

We use a standard logarithmic likelihood function based on the χ^2 distribution, calculated by comparing the CO flux in each pixel of the three-dimensional data cube D_{xyv} (which has size $N_x \times N_y$ in the spatial direction and N_v in the spectral direction) with that in the model M_{xyv}. The inverse covariance matrix, as described above, is used to compute the log-likelihood ($\mathcal{L}$) in the standard way (see e.g. equation 18 in Cappellari 2017),

$$\delta_{xyv} \equiv D_{xyv} - M_{xyv}, \tag{9}$$

$$\chi^2 = \sum_{i=0}^{N_v} \delta_{xyi}^T \, \mathfrak{C}^{-1} \, \delta_{xyi}, \tag{10}$$

$$\mathcal{L} = -\frac{1}{2}(\chi^2 - N_x N_y N_v). \tag{11}$$

It is this likelihood that we minimize in our fitting procedure.

4.2.2 *Fitting process*

To ensure our kinematic fitting process converges, we set reasonable priors on some of the parameters. These are listed in Table 2. The kinematic centre of the galaxy was constrained to lie within two beamwidths of the optical galaxy centre position. The systemic velocity was allowed to vary by ± 20 km s^{-1} from that found by optical analyses. The gas velocity dispersion was constrained to be less than 30 km s^{-1} and the disc scalelength was constrained to be less than 10 arcsec. The M/L was allowed to vary between 0.1 and 4.0 $\mathrm{M}_\odot/\mathrm{L}_{\odot,i}$. The inclination of the gas disc was allowed to vary over the full physical range allowed by the MGE model. Good fits were always found well within these ranges. A flat prior was used for each of these parameters (an assumption of maximal ignorance). The prior on the SMBH mass was flat in log-space, with the mass allowed to vary between $\log_{10}(\frac{M_{\mathrm{BH}}}{\mathrm{M}_\odot}) = 4.8$ and 9.8.

Once the MCMC chains converged, we ran the best chain 10^5 steps (with a 10 per cent burn-in) to produce our final posterior probability distribution. For each model parameter, these probability surfaces were then marginalized over to produce a best-fitting value (median of the marginalized posterior distribution) and associated 68 and 99 per cent confidence levels (CL). These are also listed in Table 2. Fig. 6 shows the one- and two-dimensional marginalizations of the physical galaxy parameters (i.e. not the kinematic centre and luminosity scaling, which are nuisance parameters). We note that the gas velocity dispersion is very low and not well constrained by our data, hence the clipping at the low end of our prior visible in those panels. This is discussed in more detail in Section 4.3.

We clearly detect the presence of a massive dark object in the centre of NGC 4697, with a mass of $(1.3^{+0.18}_{-0.14}) \times 10^8$ $\mathrm{M}_\odot$ (at the 99 per cent CL). The best-fitting i-band M/L is $2.14^{+0.04}_{-0.05}$ $\mathrm{M}_\odot/\mathrm{L}_{\odot,i}$. We note that the uncertainties quoted here include random errors only, but we discuss systematic sources of uncertainty in Section 5. The best model is an excellent fit ($\chi^2_{\mathrm{red}} = 1.02$). Fig. 7 compares the moments extracted from our best-fitting KINMS model to those observed. Fig. 8 shows the observed PVD overplotted with the best-fitting model, and with models with no SMBH and an overly large SMBH. An SMBH is clearly required to match the Keplerian uptick in velocity around the centre of the galaxy, and the majority of the structure shown in the data can be reproduced by our simple model.

4.3 Main uncertainties

In this section, we consider the main uncertainties that could affect the results derived above. These can roughly be divided into two subsets: issues with the modelling process and breakdown of the simplifying assumptions made.

4.3.1 *Luminous mass models, AGN and dust*

We use MGE models of the stellar light distribution to model the contribution of luminous matter to the observed gas kinematics. However, it is possible for these models to be contaminated, which would lead to an under/overestimate of the stellar luminosity in some parts of our object, and thus bias the derived parameters.

The first of these contaminants is optically obscuring dust that is ubiquitously present in ETGs with molecular gas (Alatalo et al. 2013). To minimize dust extinction, our MGE models were constructed from *HST F814LP* images (the longest wavelength available). The models are also carefully fitted to avoid any contamination from extinction still visible in the image (via masking of affected regions). This has been shown to work well to recover the intrinsic light distribution of such systems (Cappellari 2002). In addition, we are helped by the fact that the very centre of the galaxy appears relatively extinction free. Dust is present in the outer parts of the molecular disc, however, where the M/L is primarily constrained. If anything, we thus expect that residual dust extinction would cause our dynamical M/L to be biased to high values, and in turn the SMBH mass to be underestimated.

A second potential issue is that we have assumed that the M/L of the stellar population is constant within our field of view. In objects with molecular gas and star formation, this may not, however, be strictly correct. Davis & McDermid (2017) addressed this issue in some detail and found that, if present, M/L gradients in molecular gas-hosting ETGs like NGC 4697 are generally very shallow, due to the low mass fraction of young stars. This is especially likely to be the case in NGC 4697 given its very low SFR. This suggests that any effect from a variable M/L will be small. If any effect is present, then the SMBH mass we derive will in any case be a lower limit (as any star formation would lead to an M/L in the galaxy centre lower than we have estimated here, so a larger SMBH would be required to reproduce the same kinematics).

Despite the care taken, the possibility remains that the observational uncertainties and systematics discussed above affect the measurement of our parameters. In addition, there are uncertainties inherent to the construction of the MGE model itself. To test the sensitivity of our result to such errors, we re-ran our fitting procedure assuming that our MGE model over/underestimated the circular velocity at each radius by ± 10 per cent. In reality, such errors would

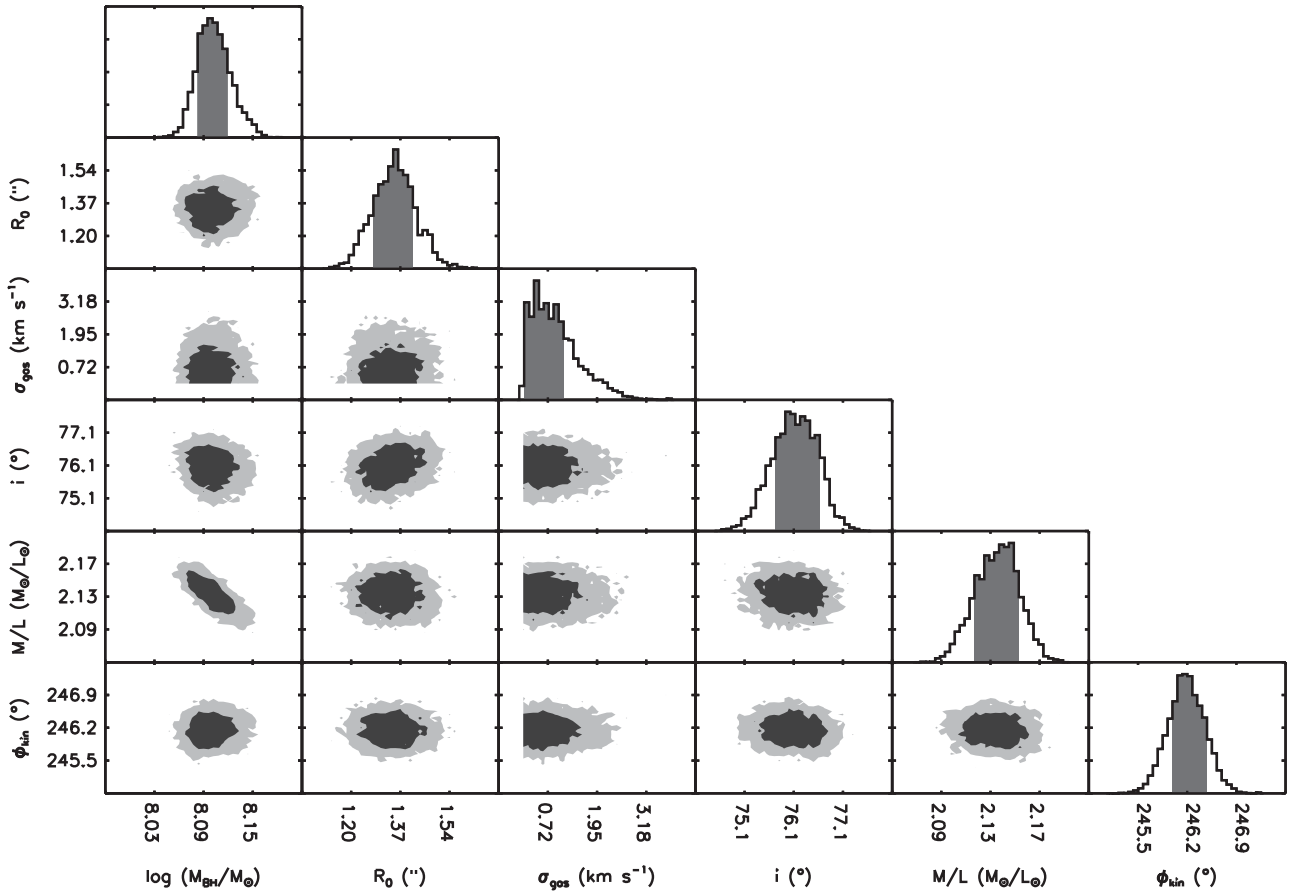

Figure 6. Visualization of the multidimensional parameter space explored by our fitting procedure for the most important (i.e. physical) fit parameters. In the top panel of each column, a one-dimensional histogram shows the marginalized posterior distribution of that given parameter, with the 68 per cent (1σ) confidence interval shaded in dark grey. In the panels below, the grey-scale shows the two-dimensional marginalizations of those fitted parameters. Regions of parameter space within the 99 per cent confidence interval are coloured in pale grey, while regions within the 68 per cent confidence interval are coloured in dark grey. See Table 2 for a quantitative description of the likelihoods.

be expected to affect the rotation curve differently at different radii, but we have no a priori way of knowing which variations to test, and a Monte Carlo approach is prohibitively time-consuming. This approach thus attempts to show the maximum expected variation, and yields a simple estimate of the sensitivity of our fit to such errors. The value of ± 10 per cent is chosen arbitrarily, but it does reflect the typical errors assumed in MGE modelling by other authors (see e.g. Davis et al. 2013b).

As expected, forcing a variation in the circular velocity by ± 10 per cent changed our best-fitting *M*/*L* significantly, to 1.7 and 2.6 $M_\odot/L_{\odot,i}$. Despite these large changes in *M*/*L*, the SMBH mass we derive remains constant at $(1.3^{+0.18}_{-0.14}) \times 10^8$ $M_\odot$. This is because we resolve the Keplerian velocity increase in the galaxy centre, which provides *M*/*L*-independent information on the SMBH mass. We thus consider our SMBH mass estimate robust to reasonable systematic errors in our mass models (including *M*/*L* gradients and dust extinction).

All SMBH mass estimates are systematically affected by the distance they assume to their target galaxy (with $M_{\rm BH} \propto D$). Here we used an SBF distance from Tonry et al. (2001), which has a formal uncertainty of $\approx$10 per cent. Thus, the systematic distance uncertainties on the SMBH mass are of a similar order as our random uncertainties.

A further possible contaminant in our target is the AGN. NGC 4697 does have some central radio emission and a nuclear hard X-ray source that suggest ongoing low-level accretion. A nuclear point source is also found in our optical image. As mentioned above, we attempted to remove the contribution of the AGN to the light by removing the central spatially unresolved Gaussian from our MGE model, mimicking point spread function subtraction. However, including this point source in the stellar light model would only yield a slightly lower SMBH mass of $(9.3^{+1.8}_{-1.4}) \times 10^7$ $M_\odot$. We include this additional 0.1 dex contribution to the SMBH mass error budget, which becomes $(1.3^{+0.18}_{-0.17}) \times 10^8$ $M_\odot$.

4.3.2 *Non-circular motions*

As previously discussed, in our analysis we assume that the gas in NGC 4697 is in purely circular motion. If significant non-circular motions are present (e.g. inflow, outflow, streaming), then this could affect our analysis.

Randriamampandry et al. (2015) studied the effect of non-circular motions on the derivation of mass profiles in detail, and showed that dramatic variations can be caused in strongly barred galaxies if the bar is orientated at specific angles with respect to our line of sight. However, NGC 4697 is unbarred. Non-circular motions can still be present in objects without bars, for instance because of other departures from axisymmetry in the gravitational potential (e.g. spiral arms), but such motions are low in amplitude compared to the rotation of these systems (e.g. $\approx$10 km s^{-1} in M51, a galaxy with

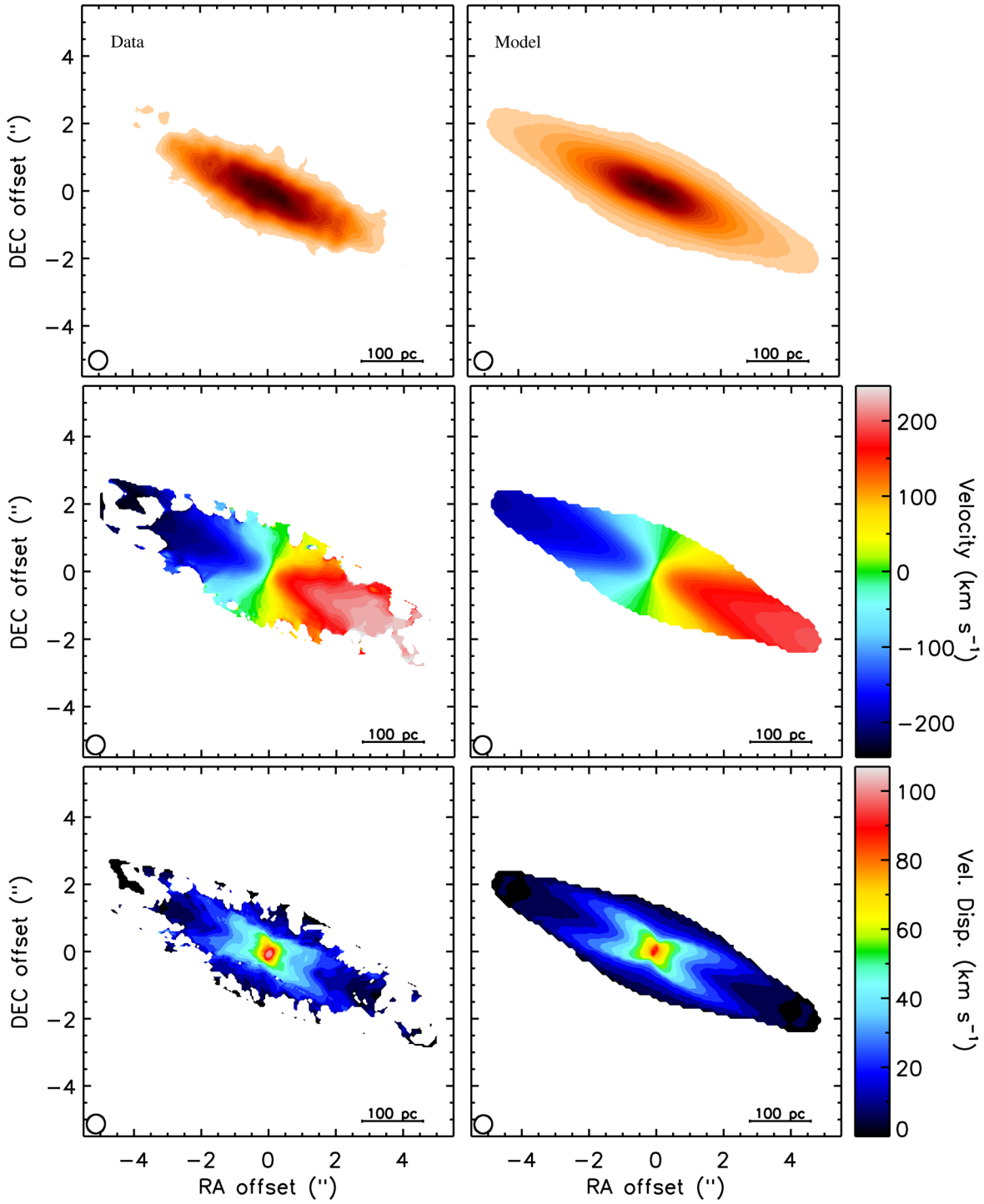

Figure 7. Integrated intensity, mean velocity and velocity dispersion maps of the ^{12}CO(2–1) emission in NGC 4697. The moments extracted from the observations are shown in the left-hand panels, while the same moments extracted in an identical way from our best-fitting model are shown in the right-hand panels.

much stronger spiral structure than early-types; Meidt et al. 2013). In addition, our *HST* images show no sign of non-axisymmetric structures in the stellar mass of this galaxy, suggesting that any such structure would have to be purely gaseous (and thus weak). Furthermore, the best-fitting model we present here does not show any major departure when compared to the data (see Figs 7 and A1), suggesting that there is no significant non-circular motion within the disc.

4.3.3 Gas velocity dispersion

In addition to non-circular motions, the molecular gas velocity dispersion provides an additional source of uncertainty (see Barth et al. 2016a). In the models presented here, we allow for a single characteristic velocity dispersion within the disc. The uncertainty in this measurement is marginalized over when estimating the confidence limits of the other parameters. However, as mentioned

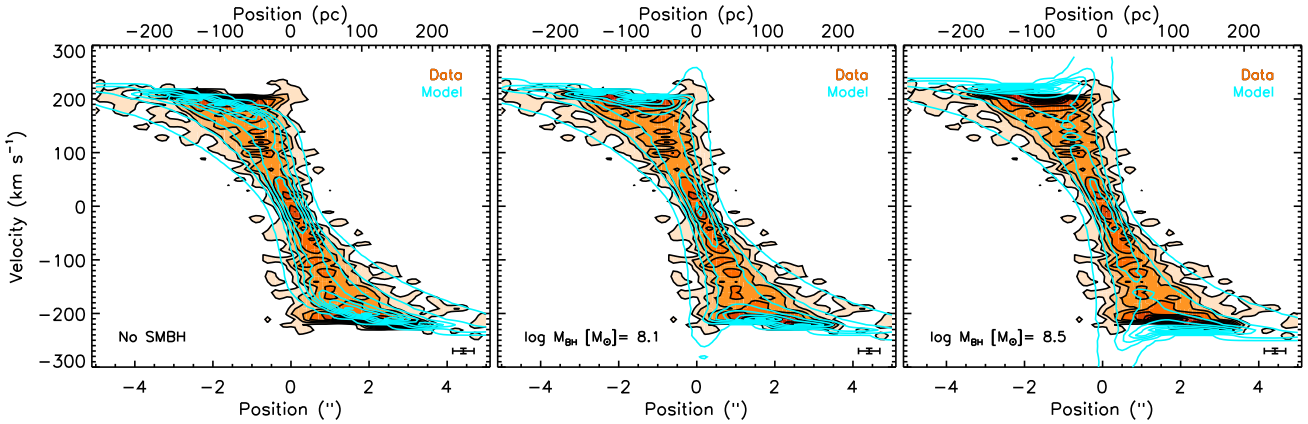

Figure 8. As Fig. 2, but overlaid with model PVDs extracted in an identical fashion from models that only differ by the central SMBH mass (blue contours). The left-hand panel has no SMBH, the centre panel shows our best-fitting SMBH mass and the right-hand panel has an overly massive SMBH. The legend of each panel indicates the exact SMBH mass used. A model with no SMBH is clearly not a good fit to the data.

in Section 3, our best-fitting value for the velocity dispersion is $\sigma_{\rm gas} \approx 0.8$ km s^{-1}, not well constrained given our channel width of 10 km s^{-1}. The ability to constrain the velocity dispersion from interferometric observations depends both on the channel width and on the signal-to-noise ratio (*S*/*N*) of the line detection. In the case of a moderate *S*/*N*, the smallest dispersion one can constrain is approximately $2\sqrt{2\ln 2}$ times smaller than the channel width, or 4.2 km s^{-1} for our data.

To investigate what the true gas velocity dispersion is, we re-reduced our ALMA data with a channel width of 3 km s^{-1}. This width is approximately twice the raw spectral resolution, the smallest size usable if one wishes to avoid correlations between pixels in neighbouring channels (due to the Hanning smoothing applied by the ALMA pipeline). At this velocity resolution, we can constrain $\sigma_{\rm gas}$ if it is larger than 1.3 km s^{-1}. Emission is still clearly detected in this cube with an rms of 2.1 mJy beam^{-1}. The clear channelization of the velocity field is also still present, suggesting that the velocity dispersion truly is very low.

We repeated the kinematic fitting described above (see Section 4.2) on this higher velocity resolution cube. These fits were able to better constrain the velocity dispersion, yielding a value of $1.65^{+0.68}_{-0.65}$ km s^{-1} (at the 99 per cent CL). We note that adopting this slightly higher value does not affect the results presented in Table 2. We nevertheless discuss this surprisingly low velocity dispersion further in Section 5.2.

In all the analyses above, we assumed that the gas velocity dispersion was spatially constant. In reality, the velocity dispersion could vary with radius and azimuth within the gas disc. In the central part of the galaxy, where beam smearing is important, an increase in velocity dispersion could lead to an SMBH mass overestimate.

To quantify the size of this effect, we re-ran the modelling process for NGC 4697, allowing for a variable velocity dispersion as a function of radius. When we allow for a linear gradient in velocity dispersion, we find the same low velocity dispersion values and a marginally negative slope, consistent with zero. To completely remove the SMBH kinematic signature and simultaneously reproduce our data, the velocity dispersion of the gas would have to increase by a factor of 50, from <2 km s^{-1} outside a galactocentric radius of $\approx$50 pc to over 130 km s^{-1} inside our inner resolution element. We consider this highly unlikely.

While the velocity dispersions of clouds in the centre of the Milky Way are larger than those of clouds in the disc, and several individual colliding clouds do have large line widths, when averaged by volume one would typically expect an enhancement of only a factor of $\approx$2 (e.g. Kumar & Riffert 1997). Even a factor of 20 increase over our measured disc average velocity dispersion would have a negligible effect on our measured parameters. We thus consider them robust again such a change.

4.3.4 *Gas mass*

In addition to luminous matter, the mass of any interstellar material present also contributes to the total dynamical mass of a galaxy. As we measure the CO line in this work, we could in principle include the molecular gas mass density in our mass models. However, given the uncertainty in $X_{\rm CO}$ (the conversion between ^{12}CO(1–0) luminosity and mass) and the ^{12}CO(1–0)/^{12}CO(2–1) ratio, this would add additional uncertainty, especially in objects with high gas fractions.

Luckily, due to their low gas fractions, in ETGs the molecular reservoirs are usually dynamically unimportant (see e.g. Davis & McDermid 2017). This is certainly true here, where the total H_2 mass over the entire molecular gas disc is only $\approx 10^7$ $M_\odot$ (assuming a standard Galactic conversion factor). Our mass model suggests a stellar mass of $\approx 2 \times 10^9$ $M_\odot$ within 200 pc of the centre of NGC 4697, two orders of magnitude greater than the molecular gas mass in the same region. Additionally, the total molecular gas mass is only a 10th of the SMBH mass. The H_2 mass within our inner resolution element (i.e. around the SMBH) is even less (a few times 10^6 $M_\odot$ of molecular gas is seen in projection against the nucleus). We note that no information is available on the H I mass of NGC 4697, but we consider it unlikely that this substantially biases our results, as the inner parts of massive ETGs are always molecular gas dominated when both phases are present (Serra et al. 2012; Davis et al. 2014). We thus consider it unlikely that neglecting the mass of gas in our fitting procedure significantly biases our results.

5 DISCUSSION

In this paper, we presented ALMA ^{12}CO(2–1) observations of the nearby fast rotator NGC 4697. We showed that it hosts a small molecular gas disc, co-spatial with a dust disc that we also mapped in thermal dust emission. We then used the observed gas kinematics to estimate the mass of the central SMBH, along with other galaxy parameters. In this section, we compare our results to those of other authors and discuss several additional issues.

5.1 Molecular gas mass

In Section 3, we estimated that the molecular gas mass present in NGC 4697 is $(1.62 \pm 0.17) \times 10^7$ $M_\odot$. This object has not been interferometrically mapped before, but it was observed with the single-dish Institut de Radioastronomie Millimétrique 30 m telescope by Young et al. (2011). These authors did not detect ^{12}CO(1–0) or ^{12}CO(2–1) in NGC 4697, and set a 3σ upper limit of $(7 \pm 2.4) \times 10^6$ $M_\odot$ of molecular gas (using the same standard X_{CO} and distance as we do in Section 3). However, they assumed a velocity width of 300 km s^{-1}, while here we detect emission over $\approx$480 km s^{-1}. Correcting the estimate of Young et al. (2011) for this larger line width yields an upper limit of $(1.2 \pm 0.4) \times 10^7$ $M_\odot$ of molecular gas, consistent within the errors with the value estimated from our ALMA data.

5.2 Gas velocity dispersion

As discussed at some length above, the velocity dispersion in the molecular gas disc of NGC 4697 seems abnormally low. Molecular gas velocity dispersions in the Milky Way and nearby spiral galaxies are typically $\approx$6–12 km s^{-1} (e.g. Larson 1981; Caldu-Primo et al. 2013). In NGC 4697, we find a value of $1.65^{+0.68}_{-0.65}$ km s^{-1}. While there is some uncertainty in this estimate, σ_{gas} is certainly $<$3 km s^{-1}, and it does not seem to vary significantly radially. It is thus important to establish what may cause NGC 4697 to differ and have such dynamically cold gas.

Observational effects are one possibility. For instance, Caldu-Primo et al. (2013) and Caldu-Primo & Schruba (2016) show that interferometric observations can underestimate the velocity dispersion if they resolve out a smooth component of the molecular emission. We do not expect this to be the case here, however, as our observations are sensitive to emission $\lesssim$300 pc, which is the total size of the dust disc visible in *HST*, and much larger than the characteristic size of giant molecular clouds (GMCs). In addition, the single-dish upper limit of Young et al. (2011) does not allow for the presence of much additional mass not detected by ALMA.

In normal spiral galaxies, it is thought that the velocity dispersion is set by a feedback loop between gravitational collapse and energy injection from star formation, in such a way that clouds stay approximately in virial equilibrium (e.g. Larson 1981; Solomon et al. 1987). One might speculate that with its low estimated SFR, NGC 4697 is simply unable to heat its molecular gas effectively. This is unlikely to be the full story, however, because although the total SFR is low, the SFR surface density within the small nuclear disc is between 0.001 and 0.017 $M_\odot$ yr^{-1} kpc^{-2}, the typical range found in spiral galaxy discs (Kennicutt 1998). In addition, a higher SFR would be expected if the gas were collapsing unopposed.

One could also postulate that there are no large GMCs in NGC 4697. The Larson (1981) relations show that larger clouds have higher velocity dispersions:

$$\left(\frac{\sigma_{gas}}{\mathrm{km\,s^{-1}}}\right) = 1.1 \left(\frac{L}{\mathrm{pc}}\right)^{0.38}, \quad (12)$$

where L is the linear extent of a cloud. GMCs have typical linear extents of 10–100 pc, and thus typical velocity dispersions of 2.6–6.3 km s^{-1}. If the GMC mass function were not fully sampled in NGC 4697, then this could help explain the low velocity dispersion. This explanation is supported by the morphology of the gas in our observations, as the disc is remarkably smooth even at our high resolution (30 pc). The object is fairly edge-on, so projection effects may be important, but given that the majority of the mass (and thus flux) is in the largest GMCs (Rosolowsky 2005), some clumpiness would be expected. Given that we do not seem to spatially resolve any clumpy cloud structure with $L > 30$ pc, equation (12) predicts that the remaining (smaller) clouds should have a velocity dispersion of $<$4 km s^{-1}, and [via another Larson (1981) relation] contain $\lesssim 10^4$ $M_\odot$ of molecular gas each.

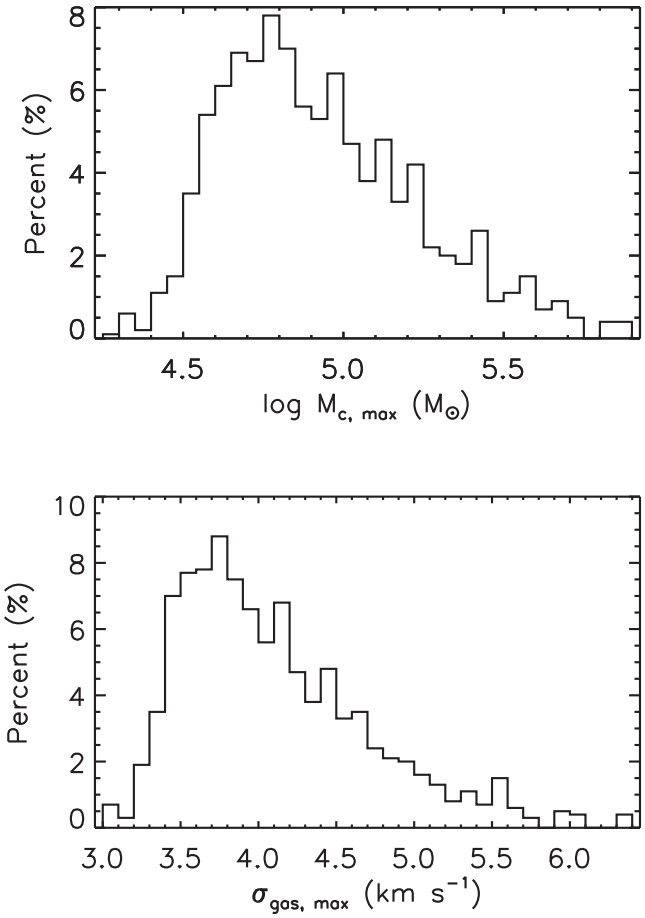

Figure 9. Top panel: likelihood of a given GMC being the largest hosted by NGC 4697 as a function of mass. Bottom panel: as above, but as a function of the cloud velocity dispersion. These maximum masses and velocity dispersions are higher than found in our observations, suggesting that other causes of the low velocity dispersion are required.

This explanation is not fully satisfying, however, as it simply shifts the question to understanding why the GMC mass function is not fully populated in NGC 4697. To address this question, we drew randomly from a typical Galactic GMC mass function (with a power-law slope of -1.75, lower mass cutoff of 100 $M_\odot$ and upper mass cutoff of 10^6 $M_\odot$; Rosolowsky 2005) to assemble a total molecular mass of 1.6×10^7 $M_\odot$. We repeated this process 10 000 times, and show in Fig. 9 histograms of the maximum cloud mass in each realization and the velocity dispersion expected from this cloud (via Larson's relations; Larson 1981). We note that in this analysis we have had to assume that the Larson (1981) relations hold in NGC 4697. Observationally, there is some evidence that this may not be the case in all environments (e.g. Bolatto et al. 2008; Heyer et al. 2009; Utomo et al. 2015). Modulo this uncertainty, we find that the median maximum cloud mass expected for a gas disc like that of NGC 4697 is 7×10^4 $M_\odot$, which equates to a velocity dispersion of 3.9 km s^{-1}. This suggests that it is quite plausible that the GMC mass function is not fully populated in this object.

On the other hand, all the realizations in our test returned a maximum velocity dispersion >3 km s^{-1}, while the observed disc in NGC 4697 seems to have a velocity dispersion even lower than this. In addition, our analysis neglects any inter-cloud velocity dispersion that (especially in an edge-on object) should act to increase the measured velocity dispersions. Thus, while it is quite likely that the GMC mass function is not fully sampled in NGC 4697, we still cannot fully explain the low dispersion observed.

Another possible explanation of this discrepancy is the hard radiation field present in NGC 4697. This system has a diffuse X-ray halo and many X-ray binaries (Sarazin et al. 2001), which along with evolved stars could mean the radiation field incident on the cold gas is much harder than that in the Milky Way. In this case, it is possible that the CO molecules are confined deeper inside the molecular clouds, in dynamically colder regions (Shetty et al. 2011; Clark & Glover 2015). We note that this scenario would also affect $X_{\rm CO}$, leading to a higher total molecular gas mass (and thus an even lower SFE).

Yet another possible explanation is the stabilizing influence of the galaxy bulge (so-called morphological quenching). Using hydrodynamic simulations, Martig et al. (2009, 2013) showed that the presence of a large bulge can stabilize a low-mass gas disc against star formation, and predicted that such stable discs would have very low velocity dispersions. This could naturally explain the low velocity dispersion of the gas in NGC 4697, and its low SFE. Further observations of galaxies with suppressed SFE would be required to confirm which, if any, of these mechanisms can explain this phenomenon.

5.3 Comparison of SMBH mass with other measurements

In earlier sections, we estimated a mass of $(1.3^{+0.18}_{-0.17}) \times 10^8$ M$_\odot$ for the SMBH in the centre of NGC 4697. As mentioned in the introduction, the SMBH mass in this object has already been measured from observations of the galaxy's stellar kinematics. It is thus instructive to compare these other estimates to ours, to quantify systematics and uncertainties.

Gebhardt et al. (2003) found $M_{\rm BH} = (1.6 \pm 0.2) \times 10^8$ M$_\odot$ from Schwarzschild modelling of the stellar kinematics in this source, while Schulze & Gebhardt (2011) used the same technique but added a model dark matter halo and obtained the same value, $(1.6 \pm 0.5) \times 10^8$ M$_\odot$. These authors both used slightly different distances, which we homogenized to our value here (assuming $M_{\rm BH} \propto D$).

The value we have derived is in excellent agreement with these literature measurements. This is despite the very different systematics involved. For instance, Gebhardt et al. (2003) and Schulze & Gebhardt (2011) used Schwarzschild modelling of the stellar kinematics to estimate the SMBH mass. This method is very different, both conceptually and numerically, from the technique used here. In addition, both these authors used *HST F555W* observations to construct their mass models, while we used *F850LP*. They also only had access to long-slit spectroscopy when modelling the stellar kinematics, while we had full three-dimensional data. Overall, this agreement between different methods, using very different tracers, is highly encouraging for the field.

5.4 SMBH mass–galaxy correlations

Individual estimates of SMBH masses are interesting, but it is their variations with galaxy properties that motivate the WISDOM project. In Fig. 10, we show the location of our object on the $M_{\rm BH}$–σ_* stellar velocity dispersion (σ_*) relation, using the compiled SMBH masses from McConnell & Ma (2013). NGC 4697 is in red, and all of the other recent SMBH mass measurements using molecular gas are in blue (Davis et al. 2013b; Onishi et al. 2015, 2017; Barth et al. 2016a). NGC 4697 lies slightly above the best-fitting $M_{\rm BH}$–σ_* relation of McConnell & Ma (2013), but well within the scatter.

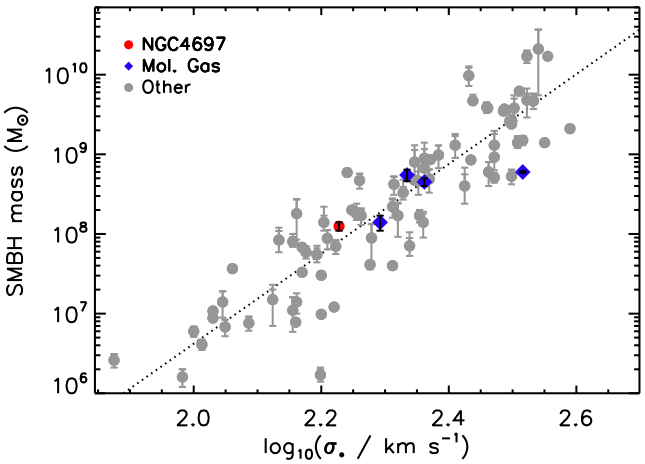

Figure 10. $M_{\rm BH}$–σ_* relation from the compilation of McConnell & Ma (2013, grey points and dotted line). We also show the SMBH mass measured for NGC 4697 in this paper as a red circle and highlight measurements from other works also using the molecular gas technique with blue diamonds.

NGC 4697 is only the fifth object studied to date using molecular gas, and it has the lowest SMBH mass studied thus far. Four of these objects seem to cluster tightly around the best-fitting $M_{\rm BH}$–σ_* relation of McConnell & Ma (2013), while the fifth (NGC 1332) falls below, at the outer edge of the scatter. It is hard to make strong statements about the importance of this without better statistics. We note, however, that the relatively small errors of these measurements are highly promising for studies of the intrinsic scatter in the SMBH–galaxy relations.

6 CONCLUSIONS

In this paper, we have presented ALMA ^{12}CO(2–1) observations of the nearby fast-rotating ETG NGC 4697, taken as part of the WISDOM project. This galaxy hosts a small central molecular gas disc, co-spatial with an obscuring dust disc visible in *HST* imaging, and containing $(1.62 \pm 0.01 \pm 0.36) \times 10^7$ M$_\odot$ of molecular hydrogen assuming a Galactic $X_{\rm CO}$ factor. We also detected spatially resolved 1 mm continuum emission from this disc, which seems to be dominated by the Rayleigh–Jeans tail of the thermal emission from dust. We used this emission, along with data from the literature, to estimate a dust mass of $(2.8 \pm 0.2 \pm 1.0) \times 10^5$ M$_\odot$, a dust temperature of 28.7 ± 0.4 K and a molecular gas-to-dust ratio of 58 ± 7.

The PVD extracted along the major axis NGC 4697 shows a Keplerian increase of the rotation velocity inside the SOI of the central SMBH. A forward modelling approach in a Bayesian framework was used to fit the observed data cube of NG4697 and estimate the SMBH mass, stellar M/L and numerous parameters describing the structure of the molecular gas disc. We found that the SMBH in this galaxy has a mass of $(1.3^{+0.18}_{-0.17}) \times 10^8$ M$_\odot$ (at the 99 per cent CL) and the i-band M/L is $2.14^{+0.04}_{-0.05}$ M$_\odot$/L$_\odot$. The inclination of the system is constrained to be $76^\circ \pm 1.^\circ 1$. With this SMBH mass, NGC 4697 lies slightly above the best-fitting $M_{\rm BH}$–σ_* relation of McConnell & Ma (2013), but well within the scatter.

NGC 4697 was found to have a very low molecular gas velocity dispersion. Part of the explanation is likely that the GMC mass function is not fully sampled in objects with such low H_2 masses. This interpretation is supported by the lack of spatially resolved structure in the integrated intensity map of NGC 4697. However, other physical mechanisms are probably required to explain the low dispersion in this object. It is possible that CO molecules are confined deeper inside the molecular clouds by a hard radiation field, or that the large bulge of this system stabilizes the gas disc (as expected from simulations of morphological quenching).

As a technique in its infancy, it is important to cross-check the results of molecular gas SMBH mass estimates with those made using other techniques. For NGC 4697, we find that our estimate of the SMBH mass is entirely consistent with previous measurements using stellar kinematics. This is despite these studies using a different technique and completely different data. This is in contrast to NGC 1332, where Barth et al. (2016a,b) used molecular gas kinematics to find an SMBH mass significantly lower than that estimated using stellar kinematics. Larger samples with SMBH masses derived from both molecular gas dynamics and stellar dynamics are clearly required to understand this discrepancy. In addition, cross-checks with other techniques such as ionized gas and maser SMBH mass measurements will be important. In this way, we can build on the promising results of this work and allow molecular gas SMBH mass estimates to be used with confidence in the ALMA era.

ACKNOWLEDGEMENTS

TAD acknowledges support from a Science and Technology Facilities Council Ernest Rutherford Fellowship, and thanks F. van de Voort for useful discussions and comments on early versions of this manuscript. MB was supported by the consolidated grants 'Astrophysics at Oxford' ST/H002456/1 and ST/K00106X/1 from the UK Research Council. MC acknowledges support from a Royal Society University Research Fellowship.

This paper makes use of the following ALMA data: ADS/JAO.ALMA#2015.1.00598.S. ALMA is a partnership of ESO (representing its member states), NSF (USA) and NINS (Japan), together with NRC (Canada), NSC and ASIAA (Taiwan) and KASI (Republic of Korea), in cooperation with the Republic of Chile. The Joint ALMA Observatory is operated by ESO, AUI/NRAO and NAOJ.

This paper also makes use of observations made with the NASA/ESA *Hubble Space Telescope*, and obtained from the Hubble Legacy Archive, which is a collaboration between the Space Telescope Science Institute (STScI/NASA), the Space Telescope European Coordinating Facility (ST-ECF/ESA) and the Canadian Astronomy Data Centre (CADC/NRC/CSA). This research has made use of the NASA/IPAC Extragalactic Database (NED) which is operated by the Jet Propulsion Laboratory, California Institute of Technology, under contract with the National Aeronautics and Space Administration.

REFERENCES

Alatalo K. et al., 2013, MNRAS, 432, 1796
Barth A. J., Boizelle B. D., Darling J., Baker A. J., Buote D. A., Ho L. C., Walsh J. L., 2016a, ApJ, 822, L28
Barth A. J., Darling J., Baker A. J., Boizelle B. D., Buote D. A., Ho L. C., Walsh J. L., 2016b, ApJ, 823, 51
Bigiel F., Leroy A., Walter F., Brinks E., de Blok W. J. G., Madore B., Thornley M. D., 2008, AJ, 136, 2846
Bigiel F. et al., 2011, ApJ, 730, L13
Bolatto A. D., Leroy A. K., Rosolowsky E., Walter F., Blitz L., 2008, ApJ, 686, 948
Brown M. J. I., Jannuzi B. T., Floyd D. J. E., Mould J. R., 2011, ApJ, 731, L41
Caldu-Primo A., Schruba A., 2016, AJ, 151, 34
Caldu-Primo A., Schruba A., Walter F., Leroy A., Sandstrom K., de Blok W. J. G., Ianjamasimanana R., Mogotsi K. M., 2013, AJ, 146, 150
Cappellari M., 2002, MNRAS, 333, 400
Cappellari M., 2017, MNRAS, 466, 798
Cappellari M., Verolme E. K., van der Marel R. P., Verdoes Kleijn G. A., Illingworth G. D., Franx M., Carollo C. M., de Zeeuw P. T., 2002, ApJ, 578, 787
Cappellari M., Neumayer N., Reunanen J., van der Werf P. P., de Zeeuw P. T., Rix H. W., 2009, MNRAS, 394, 660
Cappellari M. et al., 2011, MNRAS, 413, 813
Cappellari M. et al., 2013a, MNRAS, 432, 1709
Cappellari M. et al., 2013b, MNRAS, 432, 1862
Clark P. C., Glover S. C. O., 2015, MNRAS, 452, 2057
Clark C. J. R., Schofield S. P., Gomez H. L., Davies J. I., 2016, MNRAS, 459, 1646
Condon J. J., 1992, ARA&A, 30, 575
Davis T. A., 2014, MNRAS, 443, 911
Davis T. A., McDermid R. M., 2017, MNRAS, 464, 453
Davis T. A. et al., 2013a, MNRAS, 429, 534
Davis T. A., Bureau M., Cappellari M., Sarzi M., Blitz L., 2013b, Nature, 494, 328
Davis T. A. et al., 2014, MNRAS, 444, 3427
Di Matteo T., Colberg J., Springel V., Hernquist L., Sijacki D., 2008, ApJ, 676, 33
Dressler A., Richstone D. O., 1988, ApJ, 324, 701
Emsellem E., Monnet G., Bacon R., 1994, A&A, 285, 723
Emsellem E. et al., 2011, MNRAS, 414, 888
Ferrarese L., Ford H. C., Jaffe W., 1996, ApJ, 470, 444
Ford H. A., Bregman J. N., 2013, ApJ, 770, 137
Foreman-Mackey D., Hogg D. W., Lang D., Goodman J., 2013, PASP, 125, 306
Gebhardt K. et al., 2000, ApJ, 539, L13
Gebhardt K. et al., 2003, ApJ, 583, 92
Ghez A. M. et al., 2008, ApJ, 689, 1044
Gill P. E., Murray W., Wright M. H., 1981, Practical Optimization. Academic Press, London
Gillessen S., Eisenhauer F., Trippe S., Alexander T., Genzel R., Martins F., Ott T., 2009, ApJ, 692, 1075
Graham A. W., Erwin P., Caon N., Trujillo I., 2001, ApJ, 563, L11
Greene J. E. et al., 2010, ApJ, 721, 26
Gültekin K. et al., 2009, ApJ, 698, 198
Heyer M., Krawczyk C., Duval J., Jackson J. M., 2009, ApJ, 699, 1092
Hezaveh Y. D., 2014, ApJ, 791, L41
Kennicutt R. C., 1998, ApJ, 498, 541
Kormendy J., Ho L. C., 2013, ARA&A, 51, 511
Kumar P., Riffert H., 1997, MNRAS, 292, 871
Larson R. B., 1981, MNRAS, 194, 809
McConnell N. J., Ma C.-P., 2013, ApJ, 764, 184
McGill K. L., Woo J.-H., Treu T., Malkan M. A., 2008, ApJ, 673, 703
Madore B. F., Freedman W. L., Bothun G. D., 2004, ApJ, 607, 810
Magorrian J. et al., 1998, AJ, 115, 2285
Markwardt C. B., 2009, in Bohlender D. A., Durand D., Dowler P., eds, ASP Conf. Ser. Vol. 411, Astronomical Data Analysis Software and Systems XVIII. Astron. Soc. Pac., San Francisco, p. 251
Martig M., Bournaud F., Teyssier R., Dekel A., 2009, ApJ, 707, 250
Martig M. et al., 2013, MNRAS, 432, 1914
Meidt S. E. et al., 2013, ApJ, 779, 45
Miyoshi M., Moran J., Herrnstein J., Greenhill L., Nakai N., Diamond P., Inoue M., 1995, Nature, 373, 127
Neumayer N., Cappellari M., Reunanen J., Rix H. W., van der Werf P. P., de Zeeuw P. T., Davies R. I., 2007, ApJ, 671, 1329

Nyland K. et al., 2016, MNRAS, 458, 2221
Onishi K., Iguchi S., Davis T. A., Bureau M., Cappellari M., Sarzi M., Blitz L., 2017, MNRAS, 468, 4663
Onishi K., Iguchi S., Sheth K., Kohno K., 2015, ApJ, 806, 39
Peterson B. M., Wanders I., Horne K., Collier S., Alexander T., Kaspi S., Maoz D., 1998, PASP, 110, 660
Randriamampandry T. H., Combes F., Carignan C., Deg N., 2015, MNRAS, 454, 3743
Rosolowsky E., 2005, PASP, 117, 1403
Saintonge A. et al., 2011, MNRAS, 415, 61
Sarazin C. L., Irwin J. A., Bregman J. N., 2001, ApJ, 556, 533
Sarzi M., Rix H.-W., Shields J. C., Rudnick G., Ho L. C., McIntosh D. H., Filippenko A. V., Sargent W. L. W., 2001, ApJ, 550, 65
Schawinski K., Thomas D., Sarzi M., Maraston C., Kaviraj S., Joo S.-J., Yi S. K., Silk J., 2007, MNRAS, 382, 1415
Schulze A., Gebhardt K., 2011, ApJ, 729, 21
Scott N. et al., 2013, MNRAS, 432, 1894
Serra P. et al., 2012, MNRAS, 422, 1835
Shetty R., Glover S. C., Dullemond C. P., Ostriker E. C., Harris A. I., Klessen R. S., 2011, MNRAS, 415, 3253
Silk J., Rees M. J., 1998, A&A, 331, L1
Smith M. W. L. et al., 2012, ApJ, 748, 123
Solomon P. M., Rivolo A. R., Barrett J., Yahil A., 1987, ApJ, 319, 730
Tonry J. L., Dressler A., Blakeslee J. P., Ajhar E. A., Fletcher A. B., Luppino G. A., Metzger M. R., Moore C. B., 2001, ApJ, 546, 681
Utomo D., Blitz L., Davis T., Rosolowsky E., Bureau M., Cappellari M., Sarzi M., 2015, ApJ, 803, 16
Verolme E. K. et al., 2002, MNRAS, 335, 517
Wrobel J. M., Terashima Y., Ho L. C., 2008, ApJ, 675, 1041
Young L. M. et al., 2011, MNRAS, 414, 940

APPENDIX A: CHANNEL MAPS

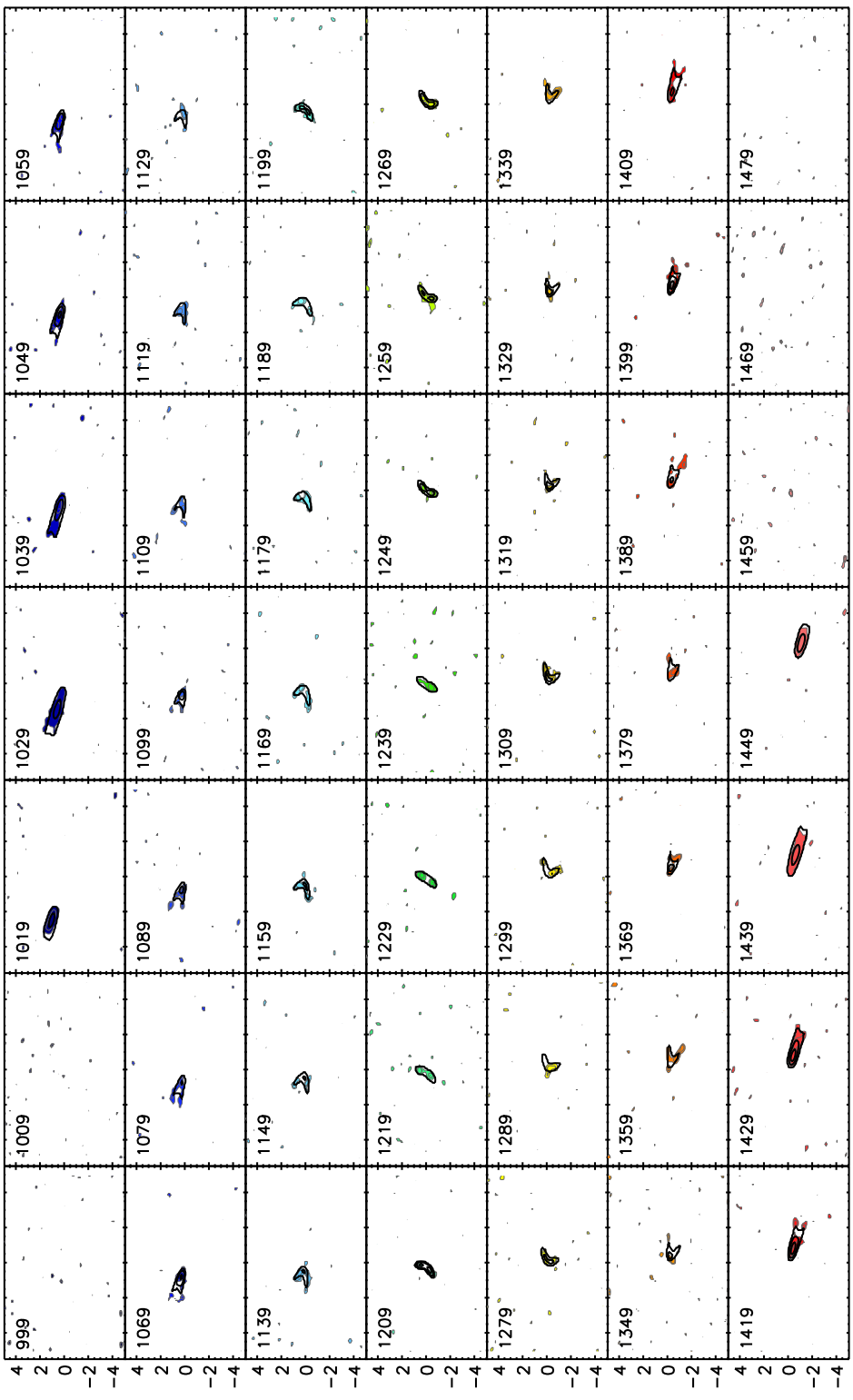

Figure A1. Channel maps of our ALMA ^{12}CO(2–1) data in the velocity range where emission is detected (1019–1449 km s^{-1}). The legend at the top left of each panel shows the velocity of that channel (in km s^{-1}). The coloured regions with grey contours show the areas detected with more than a 2.5σ significance. Overplotted on this in black are the same contour levels from our best-fitting model. Our model agrees well with the observed data in every velocity channel.

This paper has been typeset from a TEX/LATEX file prepared by the author.